A penalization method for the simulation of weakly compressible reacting gas-particle flows with general boundary conditions

Baptiste Hardy[a], Juray De Wilde[a], Grégoire Winckelmans[b]

[a] *Materials and Process Engineering, Institute of Mechanics, Materials and Civil Engineering, Université catholique de Louvain, Belgium*
[b] *Thermodynamics and Fluid Mechanics, Institute of Mechanics, Materials and Civil Engineering, Université catholique de Louvain, Belgium*

Abstract

In this paper, the Brinkman penalization method is extended to the weakly compressible formulation of the Navier-Stokes equations to study gas-particle flows with reactions and coupled heat and mass transfer. The weakly compressible approximation removes the acoustic modes from the solution while allowing a variable density. The Brinkman volume penalization method describes the solid phase as a porous medium with a vanishing permeability. The method is validated with literature benchmarks for a fixed or moving particle. Various reaction scenarios are then investigated. First, the capability of the method to deal with intra-particle diffusion and reaction is evaluated. The impact on the conversion of the particle Reynolds number based on the slip velocity is assessed, for a range of Reynolds numbers encountered in fluidization. Next, surface reactions are focused on, with infinite or finite rate. A Dirichlet-type condition is imposed on the particle surface to treat an infinite reaction rate and a high solid thermal conductivity while a finite-rate surface reaction requires Neumann and Robin surface conditions for the temperature and species mass fractions. The impact of density changes induced by heat release and molecular weight changes is assessed in these different cases. It is shown that the combination of the weakly compressible approximation and the penalization method allows to treat the presence of the solid phase and reactions in an efficient manner and to take into account the effects of compressibility in commonly encountered situations in reaction engineering.

Keywords: Penalization method, Direct Numerical Simulation, Gas-solid flows, Reacting flows, low-Mach approximation, Heat and mass transfer

Email address: baptiste.hardy@uclouvain.be (Baptiste Hardy)

1. Introduction

Gas-particle flows are encountered in a wide variety of natural phenomena and industrial applications. Among the latter, a special focus has been given to the modeling of fluidized bed reactors, due to their use in numerous processes: particle coating, base chemicals production, combustion, gasification,... Those are typically characterized by intense heat and mass transfer phenomena, in addition to complex flow structures caused by particle-particle and particle-fluid interactions. The simulation of large scale fluidized beds is typically performed by means of Two-Fluid Models (TFM), in which the solid phase is described in an Eulerian manner, or Discrete Element Methods (CFD-DEM), tracking each particle (or pseudo-particle) individually as a result of its interaction with the surrounding flow. In both approaches, closure laws are required to model the impact of the unresolved phenomena on the resolved scale of the flow. A number of correlations have been reported in the literature to obtain mass, momentum and heat transfer rates from known quantities, mostly based on experimental procedures. The weakness of these empirical correlations lies in their limited validity to mono-disperse particles, and their lack of local description [1]. Direct Numerical Simulation (DNS) of dense gas-particle flows has emerged as a powerful tool to derive closure relations based on fundamental physical grounds for the Two-Fluid and DEM-type models.

The detailed simulation of a flow with solid obstacles can be addressed in two ways: with a body conformal, or non-conformal grid. Methods based on body-fitting meshes, such as the arbitrary Lagrangian-Eulerian (ALE) finite-element method (FEM) [2], allow a straightforward treatment of the boundary conditions in the discretization process of the governing equations. Thanks to the alignment between the grid lines and the body boundaries, they also offer a better control of the grid resolution close to the body, where sharp gradients typically appear. However, the handling of more complex geometries or cases with a large fraction of the domain occupied by the dispersed phase makes the meshing process increasingly difficult. The treatment of moving bodies also requires a re-meshing at each time step and a projection of the solution onto the new grid. These two steps can drastically increase the complexity and the computational cost of the numerical method [3]. Immersed Boundary (IB) methods use non-conformal meshes. They have the advantage to use a fix grid, which reduces drastically the numerical complexity and cost of the meshing procedure. The counterpart is an increased effort to properly impose the boundary conditions on the surface of the body. The first continuous immersed boundary method was de-

veloped by Peskin [4] to simulate blood flows. IB methods are typically classified into continuous- and discrete-forcing methods. Continuous-forcing methods introduce an additional source term in the governing equations to impose the effect of the body on the fluid flow, typically using regularized delta functions. Uhlmann [5] extended Peskin's original formulation, allowing a more efficient treatment of rigid bodies. The main drawback of continuous formulations lies in the smearing of the body interface. Discrete-forcing (or sharp) IB methods, on the other hand, retain the accurate position of the interface and the forcing is introduced in the discretized form of the Navier-Stokes equations. Among those methods, the ghost-cell [6] and the cut-cell approaches [7, 8] are most widely used. The status of a ghost cell is determined from an extrapolation procedure (several schemes were derived by Majumdar [6]), and is later used in the Cartesian differentiation stencil to impose the desired boundary condition on the IB. The cut-cell (finite-volume) approach aims at guaranteeing strict local and global conservation of mass, heat and momentum by reshaping the fluid cells cut by the IB, discarding the part of the cell lying in the solid. The result of this operation is the creation of trapezoidal control volumes which leads to a finite-volume discretization of the Navier-Stokes equations. Some hybrid methods have also been developed, combining a diffuse IB method for the velocity field and a sharp interface method for the scalar fields in case of coupled mass or heat transfer between the solid and the fluid phase [9, 10].

The penalization method was first introduced by Arquis and Caltagirone [11] and belongs to the family of diffuse IB methods. In this approach, solid obstacles are modeled as porous media with vanishing permeability. Angot [12] provided a rigorous estimation of the convergence rate and error bounds for the penalization method. It was further extended to moving obstacles by Kolomenskiy et al. [13] and to scalar advection by Kadoch et al. [14]. A penalized vortex particle method was later proposed by Gazzola et al. [15] to handle deforming bodies with a non-divergence free velocity field. The penalization method has also been applied to compressible flows at both low [16] and large [17] Mach number flows.

The new methodology proposed in this paper is to couple the penalization method with the low-Mach number (or weakly compressible) approximation [18]. The low-Mach number formulation of the Navier-Stokes equations removes the acoustic modes from the solution while still allowing a variable density. This approach appears particularly interesting for the treatment of reacting

flows. Indeed, while strong temperature and species concentration gradients will appear and induce significant density fluctuations, the gas velocities are sufficiently low so that the condition $M^2 \ll 1$ is commonly satisfied. Abdelsamie et al. [19] studied two-phase turbulent reacting flows in the low-Mach approximation, using a direct-forcing IB method. Yet, the combination of the low Mach number approximation with the Brinkman penalization method appears particularly interesting for moderate Reynolds number flows. This paper presents the development of such a coupled approach as well as results obtained for general boundary conditions: Dirichlet-, Neumann- and Robin-type conditions corresponding to situations encountered in the field of reacting gas-solid flows. First, the governing equations are presented for the different types of boundary conditions. Then, the numerical method is developed and validated relatively to literature benchmarks. Finally, this new methodology is applied to the study of various situations encountered with reacting gas-solid flows, and the impact of compressibility effects is evaluated.

2. Governing equations

The computational domain Ω is split into a fluid part, Ω_f, and a solid part, Ω_s, formed by the ensemble of N_p particles

$$\Omega_s = \bigcup_{i=1}^{N_p} \Omega_{si}, \tag{1}$$

as sketched in Fig. 1.

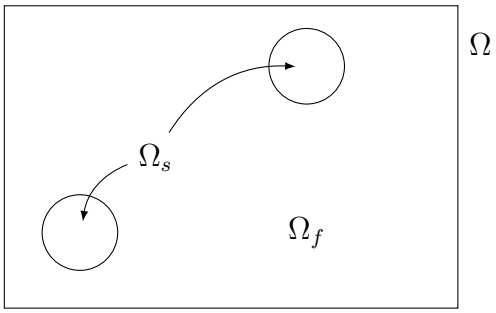


Figure 1: Sketch of the computational domain decomposition.

The fluid phase is considered as weakly compressible, i.e. acoustic modes are removed from the solution while the density is determined from the equation of state. The presence of the solid phase is treated via a Brinkman penalization method: the solid phase is tracked using a mask

function, and additional source terms are added to the fluid phase governing equations to enforce the interface boundary conditions.

We first recall the low Mach number equations for the fluid phase. The penalization method is then extended to the framework of weakly compressible flows, and for both Dirichlet and Neumann- or Robin-type boundary conditions.

2.1. The low-Mach number approximation

When the compressible Navier-Stokes equations are taken to the limit of vanishing Mach number, the weakly compressible Navier-Stokes equations are obtained (a rigorous derivation can be found in [18, 20]):

$$\frac{\partial \rho}{\partial t} + \nabla \cdot (\rho \mathbf{u}) = 0 \tag{2}$$

$$\frac{\partial (\rho \mathbf{u})}{\partial t} + \nabla \cdot (\rho \mathbf{u}\mathbf{u}) = -\nabla \tilde{p} + \nabla \cdot \boldsymbol{\tau} \tag{3}$$

$$\rho c_p \left(\frac{\partial T}{\partial t} + \mathbf{u} \cdot \nabla T \right) = \nabla \cdot (\kappa \nabla T) + \sum_{k=1}^{N_s} h_k \dot{w}_k + \frac{dp_0}{dt} \tag{4}$$

$$\rho \left(\frac{\partial Y_k}{\partial t} + \mathbf{u} \cdot \nabla Y_k \right) = -\nabla \cdot (\rho Y_k \mathbf{v}_k) - \dot{w}_k, \tag{5}$$

with the shear stress tensor, $\boldsymbol{\tau}$, defined as

$$\boldsymbol{\tau} = \mu \left(\nabla \mathbf{u} + (\nabla \mathbf{u})^T - \frac{2}{3} (\nabla \cdot \mathbf{u}) \mathbf{I} \right). \tag{6}$$

In Eqs. (2)-(6), ρ is the fluid density, $\mathbf{u}$ the velocity field, T the temperature, Y_k the mass fraction of species k ($k = 1, ..., N_s$), $\mathbf{I}$ the identity tensor, $\tilde{p}$ the dynamic pressure, p_0 the space-uniform background pressure, μ the dynamic viscosity, c_p the fluid specific heat, κ the fluid heat conductivity, h_k the enthalpy of formation of species k, $\dot{w}_k$ its volumetric consumption rate and $\mathbf{v}_k$ its diffusion velocity. Assuming that all species have equal diffusivity $\mathcal{D}$, the diffusion velocity of species k is modeled as

$$\mathbf{v}_k = -\frac{\mathcal{D}}{Y_k \overline{W}} \nabla (Y_k \overline{W}), \tag{7}$$

with $\overline{W}$ the average molecular weight of the mixture:

$$\overline{W} = \left(\sum_{k=1}^{Ns} \frac{Y_k}{W_k} \right)^{-1}. \tag{8}$$

In Eqs. (2)-(5) , the heat generated by viscous dissipation and the heat flux induced by species diffusion have been neglected.

A dimensional analysis of the compressible momentum equation shows that the spatial gradient of the pressure p is $\mathcal{O}(M^2)$ [18, 21] so that it can be decomposed as

$$p(\mathbf{x}, t) = p_0(t) + \underbrace{\tilde{p}(\mathbf{x}, t)}_{\mathcal{O}(M^2)} \tag{9}$$

where $p_0(t)$ is spatially uniform and $\tilde{p}(\mathbf{x}, t)$ is the fluctuating part of the pressure which drives the fluid dynamics. It follows from the low-Mach number approximation that the thermodynamic pressure can be linked to the temperature through the equation of state

$$p_0 = \rho T \frac{\mathcal{R}}{\overline{W}} \tag{10}$$

with $\mathcal{R}$ the universal gas constant.

When the domain has an open boundary (e.g. inflow/outflow problems), p_0 is fixed by the atmospheric conditions. In the case of a closed domain (e.g. combustion in a closed enclosure), the total mass $M_0 = \int_V \rho \, dV$ remains constant in time. Integrating both sides of Eq. (10) leads to

$$p_0 = \frac{M_0 \mathcal{R}}{\int_V \left(\frac{\overline{W}}{T} \right) dV}. \tag{11}$$

2.2. The penalization method

The volume penalization method was firstly and mostly employed to simulate incompressible flows with obstacles. It was further extended to compressible flows by Liu and Vasilyev [16]. The simple conservation of the continuity equation inside a penalized obstacle was found to cause unacceptable errors, leading these authors to propose an additional penalization on the continuity equation. Their method was limited to Dirichlet boundary conditions on the flow variables at the surface of obstacles, and it was subsequently extended by Brown-Dymkoski et al. [22] to Neumann-

and Robin-type boundary conditions. In the following, the penalization method is developed in the framework of the low-Mach number approximation, and for both Dirichlet and Neumann-Robin type surface conditions.

The solid phase is tracked through a mask function, χ:

$$\chi(\mathbf{x},t) = \begin{cases} 1 & \text{if } \mathbf{x} \in \Omega_s, \\ 0 & \text{elsewhere.} \end{cases} \tag{12}$$

2.2.1. Dirichlet boundary condition

The penalized low-Mach number equations with prescribed velocity $\mathbf{u}_s$, temperature T_s and composition $Y_{k,s}$ on the particle surface, are

$$\frac{\partial \rho}{\partial t} = -\left[1 + \chi\left(\frac{1}{\Phi} - 1\right)\right] \nabla \cdot (\rho \mathbf{u}) \tag{13}$$

$$\frac{\partial}{\partial t}(\rho \mathbf{u}) + \nabla \cdot (\rho \mathbf{u}\mathbf{u}) = -\nabla \tilde{p} + \nabla \cdot \boldsymbol{\tau} - \chi\left(\rho \frac{(\mathbf{u} - \mathbf{u}_s)}{\Delta\tau}\right) \tag{14}$$

$$\rho c_p \left(\frac{\partial T}{\partial t} + \mathbf{u} \cdot \nabla T\right) = \nabla \cdot (\kappa \nabla T) + \sum_{k=1}^{N_s} h_k \dot{w}_k + \frac{dp_0}{dt} - \chi\left(\rho c_p \frac{(T - T_s)}{\Delta\tau}\right) \tag{15}$$

$$\rho \left(\frac{\partial Y_k}{\partial t} + \mathbf{u} \cdot \nabla Y_k\right) = -\nabla \cdot (\rho Y_k \mathbf{v}_k) - \dot{w}_k - \chi\left(\rho \frac{(Y_k - Y_{k,s})}{\Delta\tau}\right) \tag{16}$$

with Φ a very small dimensionless number and $\Delta\tau$, a small number with dimensions of a time.

2.2.2. Neumann and Robin boundary condition

In [22], Brown-Dymkoski et al. introduced the so-called characteristic based volume penalization (CBVP) method for general boundary conditions by introducing hyperbolic penalization terms with inward pointing characteristics. This opened the way to more general boundary conditions on solid interfaces. In the present work, the CBVP method is extended to low Mach number Navier-Stokes equations and further used to study realistic cases such as surface reactions with heat release. In [22], the authors remove from the solution the right-hand-side containing the physical terms inside the penalized obstacle when a Dirichlet boundary condition is prescribed for one of the flow variables (e.g. no-slip condition on the velocity). We here choose to stick to the original formulation [12] and preserve the constitutive equations inside the obstacle, which ensures the smoothness of the solution, such that Eqs. (13) and (14) are unchanged. Let us now consider

the general case of a Robin-type boundary condition imposed on the scalar flow variable ϕ at the particle surface:

$$\alpha\phi + \beta\frac{\partial\phi}{\partial n} = q(\mathbf{x}, t) \tag{17}$$

with α a physical quantity with units inverse of a length and β a dimensionless quantity. The general conservation equation $\dfrac{\partial\phi}{\partial t} = \text{RHS}$, where RHS is the right-hand side of the conservation equation which governs the time variation of ϕ in the fluid phase, is penalized as

$$\frac{\partial\phi}{\partial t} = (1-\chi)\text{RHS} - \frac{\chi}{\eta_c}\left(\alpha\phi + \beta(\hat{\mathbf{n}}\cdot\nabla\phi) - q\right), \tag{18}$$

with η_c, the penalization parameter such that $1/\eta_c$ has units of a velocity. The unit normal vector to the surface, $\hat{\mathbf{n}}$, is pointing inward the obstacle to propagate information from the surface. It is defined everywhere inside the obstacle as

$$\hat{\mathbf{n}} = \frac{\nabla d}{|\nabla d|}, \tag{19}$$

where d is the distance to the surface function.
A Neumann-type boundary condition is treated identically, with $\alpha = 0$.

The penalized weakly compressible equations for general Robin-type boundary conditions on temperature and species mass fractions are then taken as

$$\frac{\partial T}{\partial t} = (1-\chi)\left(-\mathbf{u}\cdot\nabla T + \frac{1}{\rho c_p}\nabla\cdot(\kappa\nabla T) + \frac{dp_0}{dt} + \sum_{k=1}^{N_s} h_k\dot{w}_k\right) - \frac{\chi}{\eta_c}\left(\alpha_T T + \beta_T(\hat{\mathbf{n}}\cdot\nabla T) - q\right) \tag{20}$$

$$\frac{\partial Y_k}{\partial t} = (1-\chi)\left(-\mathbf{u}\cdot\nabla Y_k - \frac{1}{\rho}\nabla\cdot(\rho Y_k\mathbf{v}_k) - \dot{w}_k\right) - \frac{\chi}{\eta_c}\left(\alpha_{Y_k} Y_k + \beta_{Y_k}(\hat{\mathbf{n}}\cdot\nabla Y_k) - q_k\right). \tag{21}$$

An issue arises when closed obstacles such as cylinders or spheres are considered. Indeed, characteristics propagate information from the surface inwards, and they will meet at any interior point equidistant from two points of the surface, carrying conflicting information. This problem can be solved as described in [22] and sketched in Fig. 2: the additional hyperbolic penalization term is only added in a small region close to the surface, yet large enough to support the differentiation stencil imposing the desired condition on the particle boundary. The core region is simply governed

by artificial diffusion. The use of upwind differentiation schemes in the hyperbolic region avoids the crossing of the hyperbolic-diffusive discontinuity which would result in a strong degradation of the physical solution.

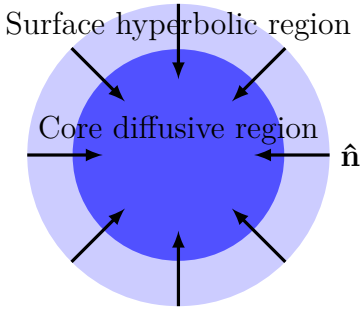


Figure 2: Sketch of the hyperbolic surface region and diffusive core region in CBVP, with inward pointing unit normal vector.

2.2.3. Coupled solid-fluid heat and mass transfer

When the interior of the solid phase undergoes a catalytic diffusion-reaction process (i.e. the reaction occurs in the solid phase only), a pseudo-continuum description of the solid phase can be adopted, and the penalization mask can be used to modify the value of the transport coefficients and source terms according to the current phase, such that Eqs. (4) and (5) are modified as

$$\frac{\partial T}{\partial t} = -\mathbf{u}\cdot\nabla T + \frac{1}{\tilde{\rho}\tilde{c}_p}\nabla\cdot(\tilde{\kappa}\nabla T) + \chi\sum_{k=1}^{N_s} h_k\dot{w}_k + (1-\chi)\frac{dp_0}{dt} \tag{22}$$

$$\frac{\partial Y_k}{\partial t} = -\mathbf{u}\cdot\nabla Y_k + \frac{1}{\rho}\nabla\cdot\left(\frac{\rho\tilde{D}}{\overline{W}}\nabla\left(Y_k\overline{W}\right)\right) - \chi\dot{w}_k \tag{23}$$

where each physical quantity "$\tilde{}$" has the value of the corresponding phase:

$$\tilde{f} = \chi f_s + (1-\chi) f \tag{24}$$

with f, the value of the quantity in the fluid phase and f_s its value in the solid phase.

2.3. Solid-phase equations

When allowed to move, each particle is tracked in a Lagrangian way by solving the Newton-Euler equations of motion:

$$m_s \dot{\mathbf{U}}_s = \mathbf{F}_{f\to s} \tag{25}$$

$$I_s \dot{\boldsymbol{\omega}}_s = \mathbf{T}_{f\to s}, \tag{26}$$

with m_s, the mass of the particle, I_s its moment of inertia, $\mathbf{U}_s$ its translational velocity and $\boldsymbol{\omega}_s$ its angular velocity. The velocity of the particle at a distance $\mathbf{r}$ from its center is then obtained as the combination of the translational and rotational contributions:

$$\mathbf{u}_s = \mathbf{U}_s + \boldsymbol{\omega}_s \times \mathbf{r}. \tag{27}$$

The interfacial force, $\mathbf{F}_{f\to s}$, and torque, $\mathbf{T}_{f\to s}$, are obtained through integration of the penalization term over the volume of the body:

$$\begin{aligned}
\mathbf{F}_{f\to s} &= -\oint_{\partial\Omega_s} \boldsymbol{\sigma}\cdot\hat{\mathbf{n}} dS \\
&= \int_{\Omega_s} \nabla\cdot\boldsymbol{\sigma} dV \\
&= \int_{\Omega_s} \rho\frac{d\mathbf{u}}{dt} dV + \int_{\Omega_s} \chi\rho\frac{(\mathbf{u}-\mathbf{u_s})}{\Delta\tau} dV \\
&= \dot{\mathbf{U}}_\mathbf{s}\int_{\Omega_s} \rho dV + \int_{\Omega_s} \chi\rho\frac{(\mathbf{u}-\mathbf{u_s})}{\Delta\tau} dV.
\end{aligned} \tag{28}$$

As detailed in [5] for the incompressible case, the rigid body assumption allows us to extract the particle acceleration, $\dot{\mathbf{U}}_\mathbf{s}$, from the first integral term, the extension to the present compressible situation is straightforward.

The interfacial torque is obtained in a similar way:

$$\begin{aligned}\mathbf{T_{f\to s}} &= -\int_{\partial\Omega_s} \mathbf{r}\times(\boldsymbol{\sigma}\cdot\hat{\mathbf{n}})\,dS \\ &= \int_{\Omega_s}(\mathbf{r}\wedge\nabla\cdot\boldsymbol{\sigma})dV \\ &= \frac{d}{dt}\int_{\Omega_s}(\mathbf{r}\wedge\rho\mathbf{u})\,dV + \int_{\Omega_s}\left(\mathbf{r}\wedge\chi\rho\frac{(\mathbf{u}-\mathbf{u_s})}{\Delta\tau}\right)dV \\ &= \dot{\boldsymbol{\omega}}_s\int_{\Omega_s}\rho r^2 dV + \int_{\Omega_s}\left(\mathbf{r}\wedge\chi\rho\frac{(\mathbf{u}-\mathbf{u_s})}{\Delta\tau}\right)dV. \end{aligned} \tag{29}$$

3. Numerical method

We use a predictor-corrector scheme to integrate the continuity equations, similar to those developed in [23, 24, 25]. As summarized in the review paper of Knikker [26], different approaches can be adopted in the sequence chosen for solving the conservation equations. In [23], Najm et al. solve the conservation equations for the density and the mass fractions before updating the temperature from the equation of state. In [24], Lessani et al. split the thermo-chemical system by solving the species continuity equations once the flow field has been advanced, assuming constant molecular weight. In this paper, the temperature and species mass fractions are first integrated. The density is subsequently obtained from state law and the velocity field can finally be updated. Second-order schemes are used for the evaluation of spatial derivatives. A classical staggered mesh is employed: the scalar quantities and the diagonal shear stresses are stored at the center of the cell, the velocities, heat and mass fluxes on the faces of the cell, and the off-diagonal shear stresses on the cell vertices.

In the following, $\mathcal{P}_\phi$ denotes the penalization source term on the quantity ϕ (temperature or species mass fraction), no matter whether it corresponds to a Dirichlet or to a Neumann-/Robin-type boundary condition.

3.1. Predictor

The predictor step uses an Adams-Bashforth scheme of or order 2 (AB2) for the time integration of the convective terms, and an Euler scheme for the diffusive and source terms, as well as for the penalization term.

1. **Integrate the energy and species transport equations**

One first computes a predictor for the temperature

$$\frac{(T^* - T^n)}{\Delta t} = \left(\frac{3}{2}C_T^n - \frac{1}{2}C_T^{n-1}\right) + \frac{1}{\rho^n c_p}\left(D_T^n + S_T^n + \frac{dp_0^n}{dt} + \mathcal{P}_T\right) \tag{30}$$

where

- $C_T = -\mathbf{u} \cdot \nabla T$
- $D_T = \nabla \cdot (\kappa \nabla T)$
- $S_T = \sum_{k=1}^{N_s} h_k \dot{w}_k$
- $\frac{dp_0^n}{dt} = \frac{p_0^n - p_0^{n-1}}{\Delta t}$.

Similarly for the species transport equation:

$$\frac{(Y_k^* - Y_k^n)}{\Delta t} = \left(\frac{3}{2}C_{Y_k}^n - \frac{1}{2}C_{Y_k}^{n-1}\right) + \frac{1}{\rho^n}\left(D_{Y_k}^n + S_{Y_k}^n + \mathcal{P}_{Y_k}\right) \tag{31}$$

where

- $C_{Y_k} = -\mathbf{u} \cdot \nabla Y_k$
- $D_{Y_k} = -\nabla \cdot (\rho Y_k \mathbf{v_k})$
- $S_{Y_k} = -\dot{w}_k$.

Then, the mean molecular weight can be updated based on Eq. (8)

2. **Update the thermodynamic pressure**

   For an open domain, $p_0^* = p_{atm}$. For a closed domain, p_0^* is deduced from Eq. (11).

3. **Update the density**.

   Use Eq. (10) to obtain ρ^* from T^* and $\overline{W}^*$

4. **Integrate the momentum equation using a two-step projection method**

   The integration of the momentum equation is based on Chorin's two-step projection method [27]. An intermediate velocity field $\hat{\mathbf{u}}$ is first computed

$$\frac{(\rho^*\hat{\mathbf{u}} - \rho^n\mathbf{u}^n)}{\Delta t} = \underbrace{\left(\frac{3}{2}{\mathbf{C}_\mathbf{u}}^n - \frac{1}{2}{\mathbf{C}_\mathbf{u}}^{n-1}\right) + \nabla \cdot \boldsymbol{\tau}^n - \nabla\tilde{p}^n}_{\triangleq \text{RHS}} - \chi\left(\frac{\rho^*(\hat{\mathbf{u}} - \mathbf{u}_s)}{\Delta\tau}\right), \tag{32}$$

where $\mathbf{C_u} = -\nabla \cdot (\rho \mathbf{u}\mathbf{u})$.

In the case of a Dirichlet boundary condition, the penalization term can be treated implicitly in a straightforward way, which allows the use of a very large ratio $\frac{\Delta t}{\Delta \tau} \gg 1$, ensuring an accurate enforcement of the boundary condition without constraining the time step to a small value. In the present work, we used a ratio $\frac{\Delta t}{\Delta \tau} = 1.0 \cdot 10^4$. The intermediate velocity field is then obtained as

$$\hat{\mathbf{u}} = \left(\left(\frac{\rho^n}{\rho^*} \right) \mathbf{u}^n + \frac{1}{\rho^*} \Delta t \, \mathrm{RHS} + \left(\frac{\Delta t}{\Delta \tau} \right) \mathbf{u_s} \right) \Big/ \left(1 + \chi \left(\frac{\Delta t}{\Delta \tau} \right) \right). \tag{33}$$

The implicit integration of the penalization term is similarly performed for scalar quantities in Eqs. (30) and (31) when a Dirichlet condition is imposed on the solid surface ($\mathcal{P}_\phi = \mathcal{P}_\phi^*$), while it is treated explicitly for Neumann- and Robin-type boundary conditions ($\mathcal{P}_\phi = \mathcal{P}_\phi^n$). The intermediate velocity field $\hat{\mathbf{u}}$ does not satisfy the continuity equation and needs to be further corrected:

$$\frac{(\rho^* \mathbf{u}^* - \rho^* \hat{\mathbf{u}})}{\Delta t} = -\nabla p', \tag{34}$$

with $p' = \tilde{p}^* - \tilde{p}^n$ the pressure correction field, obtained as the solution of a Poisson equation.

From there, the constraint coming from the continuity equation can be imposed in two ways [28]:

(a) A first approach consists in using the conservative form of the continuity equation by taking the divergence of the *momentum* ($\rho \mathbf{u}$) in order to satisfy the mass conservation constraint. This leads to a Poisson equation, requiring the evaluation of $\left(\frac{\partial \rho}{\partial t} \right)$. However, it has been reported in the literature [29, 28, 20] that the time derivative of the density is a source of instability, limiting the method to moderate density ratios.

(b) A second approach uses the continuity equation in its non-conservative form to impose the divergence of the *velocity* $\mathbf{u}$. This method turns out to be more robust and shows good stability properties when dealing with strong thermal and density gradients. The main drawback is that one needs to solve a numerically challenging variable-coefficient Poisson equation.

The first method has been used in the current work. The divergence operator is applied to both sides of Eq. (34):

$$\frac{1}{\Delta t}\left(\nabla\cdot(\rho^*\mathbf{u}^*)-\nabla\cdot(\rho^*\hat{\mathbf{u}})\right)=-\nabla^2 p'. \tag{35}$$

The first term on the left-hand side is obtained from the continuity Eq. (13),

$$\nabla\cdot(\rho^*\mathbf{u}^*)=\frac{-\left(\dfrac{\partial\rho}{\partial t}\right)^*}{\left[1+\chi\left(\dfrac{1}{\Phi}-1\right)\right]}\overset{\text{3BDF}}{=}-\frac{(3\rho^*-4\rho^n+\rho^{n-1})}{2\Delta t}\Bigg/\left[1+\chi\left(\frac{1}{\Phi}-1\right)\right], \tag{36}$$

where the time derivative of density is evaluated with a 3 points backward difference scheme (3BDF), while the second term is evaluated using the divergence of $(\rho^*\hat{\mathbf{u}})$ obtained from (32). The parameter Φ is fixed to $1.0\cdot10^{-4}$ for all subsequent simulations. The resulting Poisson equation is solved using a conjugate gradient solver preconditioned with a multi-grid method.

3.2. Corrector

If the integration is stopped after the predictor step, the method will show very poor time convergence since the predicted value for the density, ρ, is never corrected. A corrector step is hence added.

1. **Integrate the energy and species transport equations**

   For the correction step, we use a second-order "quasi Crank-Nicolson" scheme to advance the scalar quantities of the energy and species transport equations:

$$\begin{aligned}\frac{(T^{n+1}-T^n)}{\Delta t}&=\frac{1}{2}\left(C_T^n+\frac{1}{\rho^n c_p}(D_T^n+S_T^n)\right)+\frac{1}{2}\left(C_T^*+\frac{1}{\rho^* c_p}(D_T^*+S_T^*)\right)\\&\quad+\frac{1}{\rho^* c_p}\left(\frac{p_0^n-p_0^{n-1}}{\Delta t}\right)+\mathcal{P}_T\end{aligned} \tag{37}$$

$$\frac{(Y_k^{n+1}-Y_k^n)}{\Delta t}=\frac{1}{2}\left(C_{Y_k}^n+\frac{1}{\rho^{n+1}}(D_{Y_k}^n+S_{Y_k}^n)\right)+\frac{1}{2}\left(C_{Y_k}^*+\frac{1}{\rho^{n+1}}(D_{Y_k}^*+S_{Y_k}^*)\right)+\mathcal{P}_{Y_k}, \tag{38}$$

   an the mean molecular weight is subsequently updated using Eq. (8).

2. **Update the thermodynamic pressure**

   For an open domain, $p_0^{n+1}=p_{atm}$. For a closed domain, p_0^{n+1} is deduced from Eq. (11).

3. **Update the density**.

   Use Eq. (10) to obtain ρ^{n+1} from T^{n+1} and $\overline{W}^{n+1}$.

4. **Integrate the momentum equation using a two-step projection method**.

   Similarly to what was done in the predictor step, we first compute the intermediate velocity field, $\tilde{\mathbf{u}}$:

$$\frac{(\rho^{n+1}\tilde{\mathbf{u}} - \rho^n \mathbf{u}^n)}{\Delta t} = \left(\frac{3}{2}{\mathbf{C}_\mathbf{u}}^n - \frac{1}{2}{\mathbf{C}_\mathbf{u}}^{n-1}\right) + \nabla \cdot \boldsymbol{\tau}^n - \nabla \tilde{p}^n - \chi \left(\frac{\rho^{n+1}(\tilde{\mathbf{u}} - \mathbf{u}_s)}{\Delta \tau}\right) \tag{39}$$

   before enforcing the mass conservation

$$\frac{(\rho^{n+1}\mathbf{u}^{n+1} - \rho^{n+1}\tilde{\mathbf{u}})}{\Delta t} = -\nabla p', \tag{40}$$

   with $p' = \tilde{p}^{n+1} - \tilde{p}^n$, obtained as the solution of the Poisson equation

$$\frac{1}{\Delta t}\left(\nabla \cdot (\rho^{n+1}\mathbf{u}^{n+1}) - \nabla \cdot (\rho^{n+1}\tilde{\mathbf{u}})\right) = -\nabla^2 p', \tag{41}$$

   where

$$\nabla \cdot (\rho^{n+1}\mathbf{u}^{n+1}) = \frac{-\left(\dfrac{\partial \rho}{\partial t}\right)^{n+1}}{\left[1 + \chi\left(\dfrac{1}{\Phi} - 1\right)\right]} = -\frac{(3\rho^{n+1} - 4\rho^n + \rho^{n-1})}{2\Delta t} \Bigg/ \left[1 + \chi\left(\frac{1}{\Phi} - 1\right)\right]. \tag{42}$$

4. Non-reactive case studies

In order to first validate the flow part of the present methodology, some benchmark cases used for incompressible and compressible flows are reproduced using our weakly compressible code. The fluid-phase Prandtl number is $Pr = \frac{\mu_0 c_{p0}}{\kappa_0} = 0.7$, with μ_0, c_{p0} and κ_0, respectively the dynamic viscosity, specific heat and conductivity of the fluid at the reference inlet temperature T_0.

4.1. Flow past a fixed cylinder

A circular disk with diameter d_p is placed in a channel with dimensions $30d_p \times 30d_p$ and slip walls, at a distance $10d_p$ from the inflow, where a uniform velocity profile u_∞ is imposed. The

flow past the disk is computed for three different particle Reynolds number: $Re_p = \frac{\rho_0 u_\infty d_p}{\mu_0} = 40$, $Re_p = 100$ and $Re_p = 1000$, ρ_0 being the reference fluid density at T_0. Unless otherwise specified, the resolution used for all the subsequent simulations is $d_p = 30h$, with h the grid size.

4.1.1. $Re_p = 40$, $T_s = T_0$

At $Re_p = 40$, the flow is steady. If the particle temperature T_s is set equal to the reference temperature T_0 and that adiabatic conditions are imposed on the channel walls, the temperature and hence the density are uniform and constant throughout the simulation. The drag coefficient as well as different geometrical features of the flow (illustrated in Fig. 3) are extracted and compared to the literature in Table 1. Both experimental results ([30, 31]) and numerical studies have been reported. The results from the present study agree reasonably well with the reference results. The slightly high value reported for our drag coefficient with respect to other studies must be attributed to confinement effects.

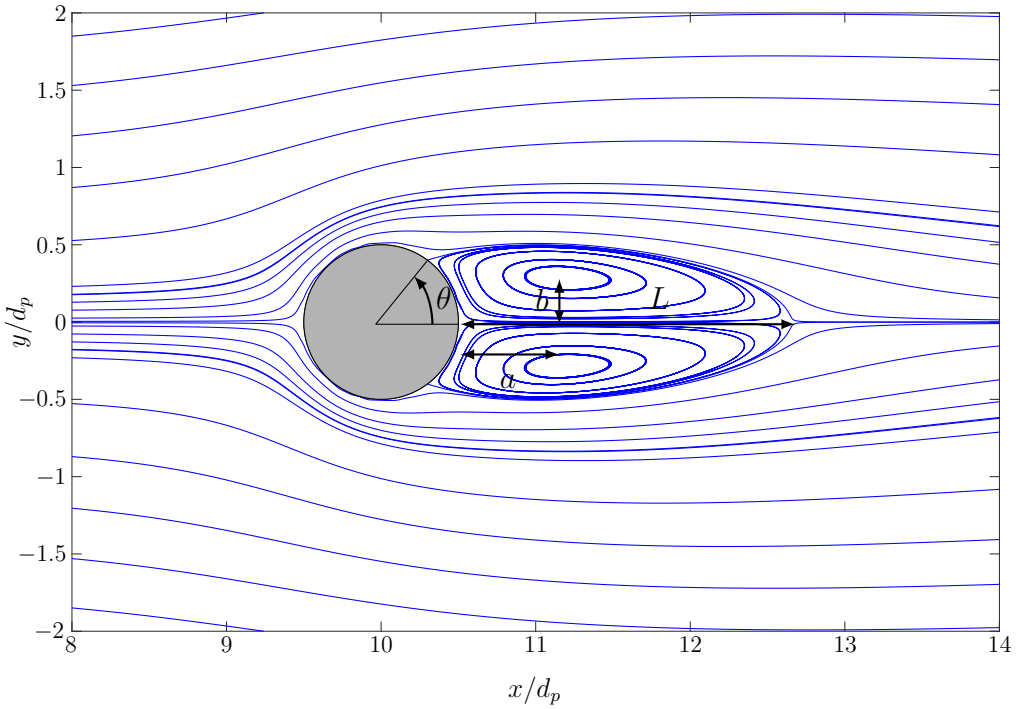


Figure 3: Streamlines of the flow past a cylinder at $Re_p = 40$ and definition of geometrical characteristics of the flow.

4.1.2. $Re_p = 40$, $T_s \neq T_0$

We here investigate the impact of the the particle surface temperature on the drag coefficient and Nusselt number. Values of drag and heat transfer coefficients in forced convection past a

Study	C_D	$\frac{a}{d_p}$	$\frac{b}{d_p}$	$\frac{L}{d_p}$	θ
Present	1.57	0.73	0.57	2.15	53.1°
Bigay et al. [32]	1.57	0.70	0.59	2.22	50.3°
Canuto & Taira [33]	1.54	0.72	0.59	2.24	53.8°
Linnick & Fasel [34]	1.52	0.72	0.60	2.28	53.6°
Denis & Chang [35]	1.52	–	–	2.35	53.8°
Tritton* [30]	1.59	–	–	–	–
Bouard & Countanceau* [31]	–	0.76	0.59	2.13	53.8°

Table 1: Flow past a fixed cylinder at $Re_p = 40$: drag coefficient and geometrical flow features. Superscript "*" indicates experimental studies.

cylinder are provided in the literature or correlated for a range of low to moderate Reynolds numbers, under the incompressible approximation. On the other hand, the effect of compressibility with non-zero Mach number flows has also been studied [36, 33] and values of drag coefficients are reported for a range of Reynolds and Mach numbers. The effect of density fluctuations resulting from temperature and composition changes on momentum, heat and mass transfer has, however, not been studied separately so far.

A set of numerical experiments has been performed with increasing values of the ratio T_s/T_0. Fig. 4 shows the extracted particle drag coefficient and Nusselt number. The Nusselt number point at $T_s/T_0 = 1$ actually corresponds to that extracted from an incompressible simulation with $T_s \neq T_0$ (since no heat transfer occurs for a unit ratio). Yet, it can be considered as the limit Nusselt number of the present weakly compressible case for a vanishing driving force. The value of the Nusselt number extracted from this incompressible simulation is $Nu = 3.257$, i.e. a difference of 2.63 % with respect to the value obtained using the Churchill-Bernstein correlation [37]:

$$\overline{Nu} = 0.3 + \frac{0.62 Re_p^{1/2} Pr^{1/3}}{[1 + (0.4/Pr)^{2/3}]^{1/4}} \left[1 + \left(\frac{Re_p}{282000}\right)^{5.8}\right]^{4/5} = 3.345. \tag{43}$$

Fig. 4 further shows that a larger ratio T_s/T_0 results in an increase of the drag and a decrease of the heat transfer coefficient, and in a quite linear way.

4.1.3. $Re_p = 100$, $T_s = T_0$

At $Re_p = 100$, the problem is unsteady with the onset of the Von-Karman vortex shedding. Once the flow has reached a statistically stationary state, the time-averaged drag coefficient $\overline{C_D}$ and the Strouhal number, $St = \frac{f_L d_p}{u_\infty}$, based on the oscillation frequency of the lift coefficient, f_L, are reported in TABLE 2, together with reference results. Again, good agreement is found, demon-

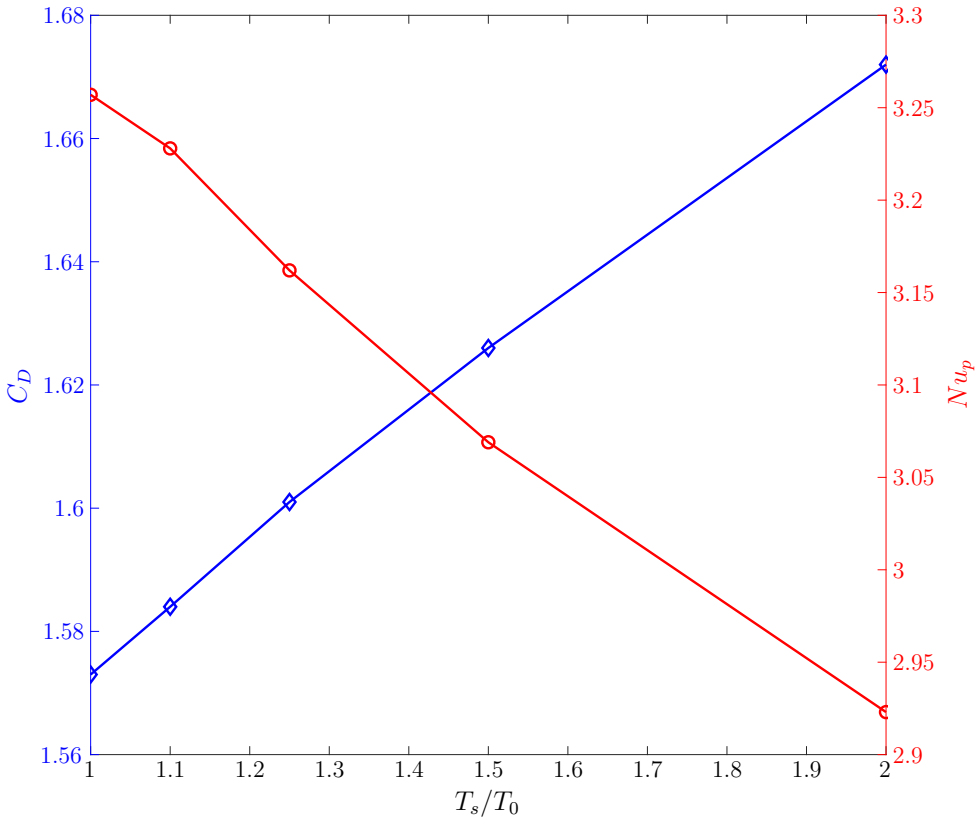


Figure 4: Evolution of the drag coefficient (−◊) and Nusselt number (−○) with the solid particle temperature.

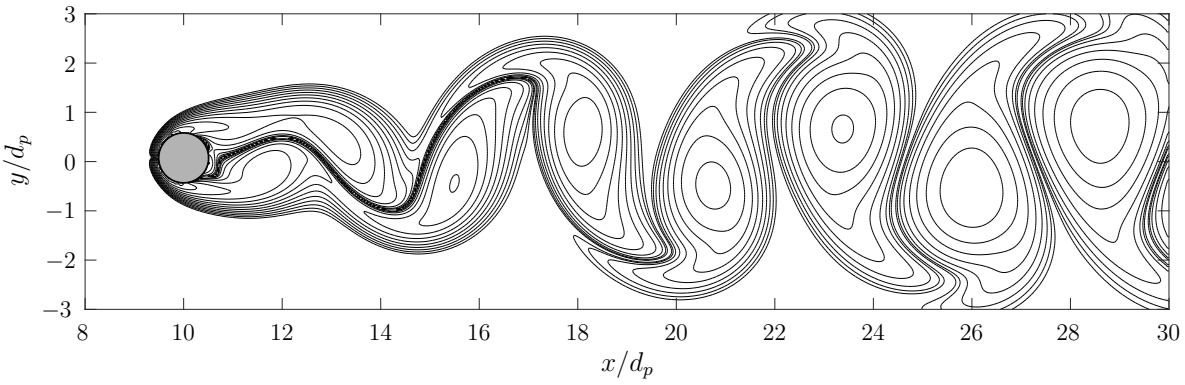
strating the ability of our method to capture accurately moderate Reynolds number unsteady flows.

Study	$\overline{C_D}$	St
Present	1.34	0.170
Canuto & Taira [33]	1.34	0.167
Mittal et al. [38]	1.35	0.165
Apte et al. [39]	1.36	0.165

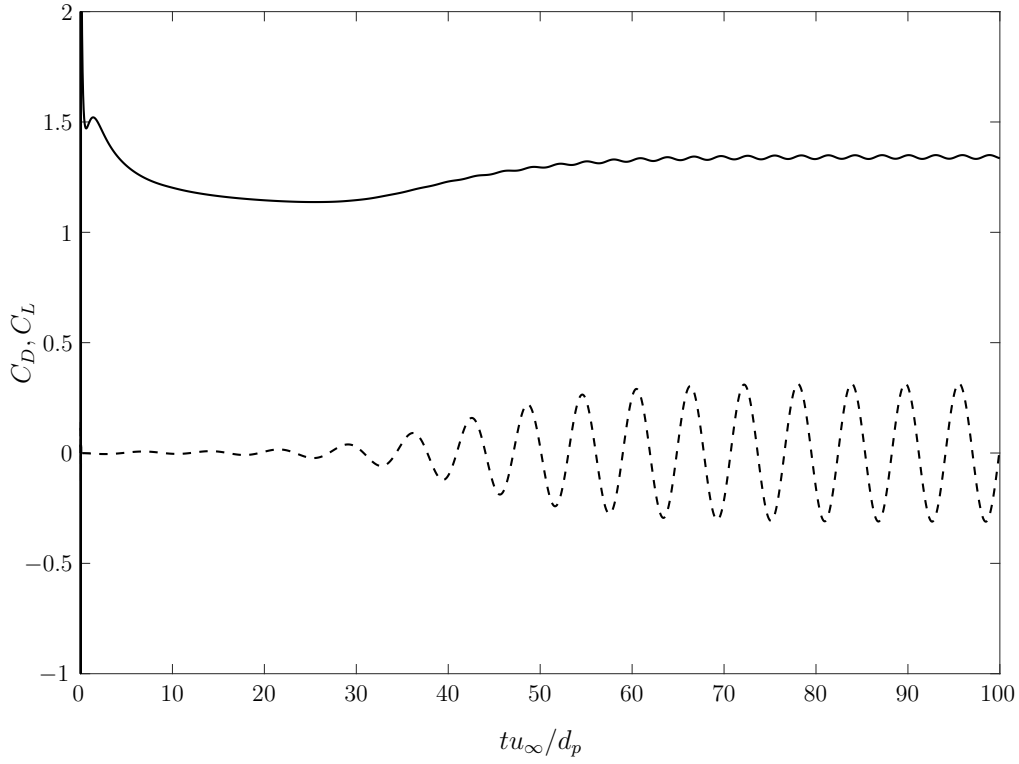
Table 2: Flow past a fixed cylinder at $Re_p = 100$: time-averaged drag coefficient and Strouhal number.

4.1.4. Heated cylinder at $Re_p = 1000$

The implementation of the CBVP method to impose Neumann- and Robin-type boundary conditions is here validated by simulating the flow past a heated cylinder at $Re_p = 1000$. A flux $\frac{\partial T}{\partial n} = 1.5\,(T_0/d_p)$ is imposed on the particle surface using Eq. (20). In their paper, Brown-Dymkoski et al. [22] use a Mach number $M = 0.20$ as they consider the fully compressible



(a)



(b)

Figure 5: Flow past a cylinder at $Re_p = 100$. (a) Iso-contours of the dimensionless vorticity $\frac{|\omega|d_p}{u_\infty} = 10^a$, with $a = -2.0, -1.75, -1.50, ..., 2.0$. (b) Time evolution of drag (solid line) and lift (dashed line) coefficients.

Navier-Stokes equations. Yet, the usual condition $M^2 \ll 1$ is still legitimate, such that the present low-Mach approximation should reproduce fairly correctly the results obtained in [22]. The domain considered has a size $[0, 12]d_p \times [-3, 3]d_p$ and the particle is positioned at $(3, 0)d_p$. The penalization parameter η_c is fixed so that $\eta_c u_\infty = 0.05$. Fig. 6a shows a close-up view of the resulting instantaneous temperature field. A vertical cut in the temperature field is extracted and plotted in Fig. 6b to verifiy the proper enforcement of the desired boundary condition $q = 1.5\, T_0/d_p$.

The time evolution of the drag and lift coefficients are given in Fig. 7. The average drag coefficient is $\overline{C_D} = 1.74$ and the Strouhal number based on the oscillation frequency of the drag coefficient is $St = 0.257$, compared to $St = 0.245$ obtained by Brown-Dymkoski et al. [22]. Our slightly higher St could be due to our stronger confinement effects and/or our lower value of $\eta_c u_\infty$.

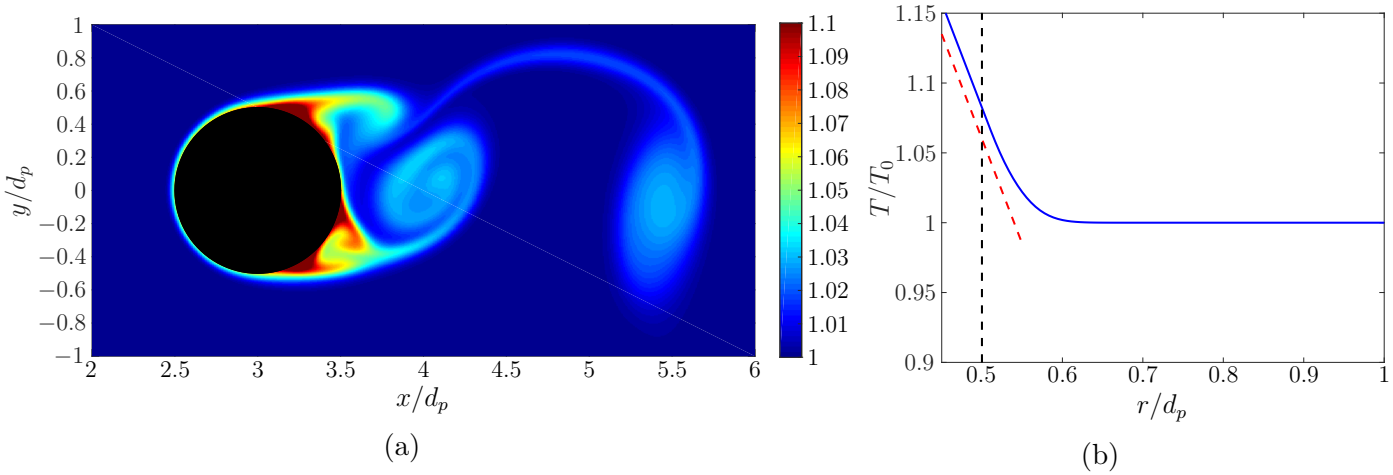


Figure 6: Dimensionless temperature field T/T_0 induced by a heat flux $q = 1.5T_0/d_p$ imposed on the particle surface. (a) Close-up view near the particle (b) Vertical cut across the particle surface (—) and comparison with a line of slope 1.5 (– –).

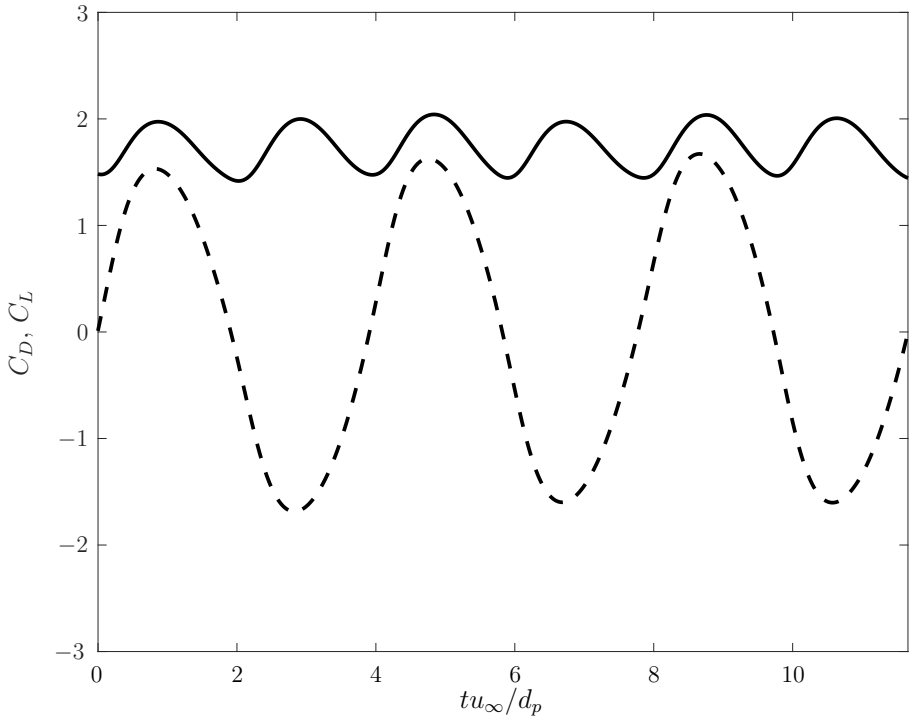
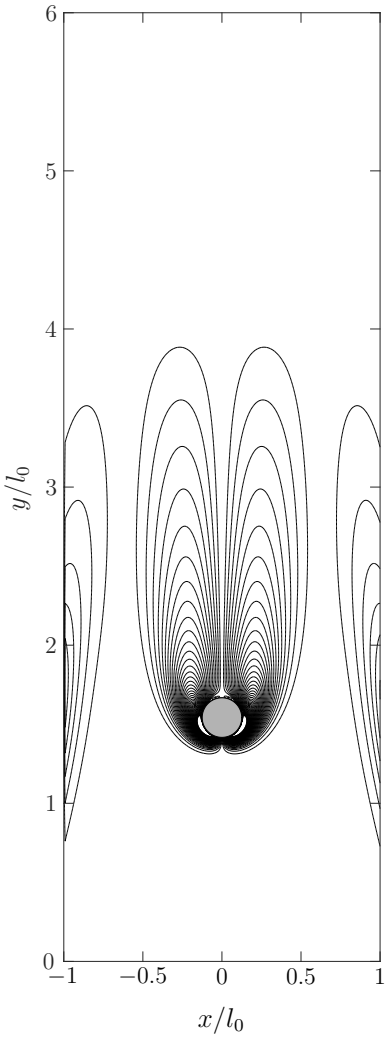


Figure 7: Drag (—) and lift coefficients (– –) past a heated cylinder at $Re_p = 1000$.

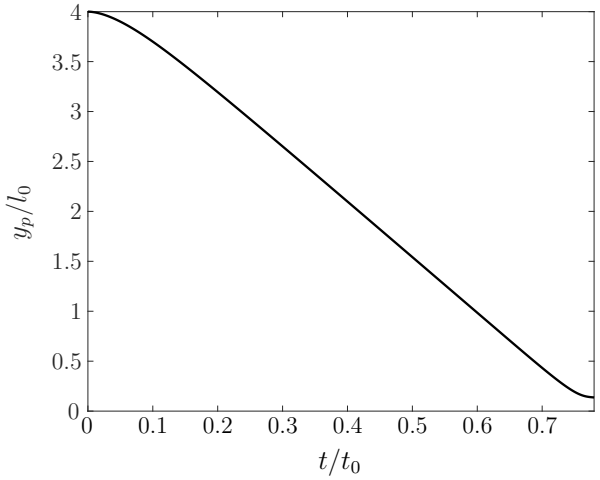
4.2. Sedimentation of a single particle

In order to validate the fluid-solid coupling of the present method, the classical test case of a cylinder sedimenting in a viscous fluid is reproduced. A no-slip condition is imposed on the walls of the channel. The cylinder accelerates under the single action of gravity until it reaches its terminal velocity, v_t. The collision of the particle with the bottom wall is part of the simulation and the collision model employed is based on repulsion forces as described by Feng and Michaelides in [40]. The geometrical and physical parameters are identical to those employed by Glowinski et al. [41] who define the reference length l_0 as the half-width of the channel, the reference velocity u_0 as $\sqrt{\frac{gl_0}{981}}$, with g the gravitational acceleration, so that the reference time is $t_0 = \frac{l_0}{u_0}$. The computational domain has a height $6\,l_0$ and the particle with diameter $d = 0.25l_0$ is initially positioned in the middle of the channel at a height $4\,l_0$. The fluid kinematic viscosity ν is set to $0.1(u_0 l_0)$ and the solid body density is $\rho_s = 1.25\rho$.

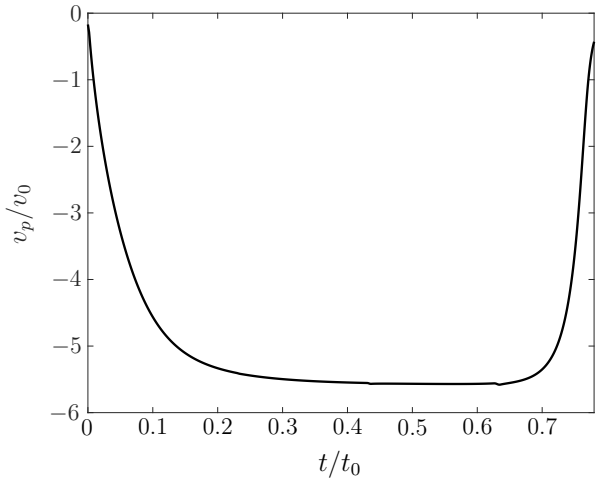
Because the density ratio between the two phases is close to one, the particle quickly reaches its terminal velocity, as evidenced in Fig. 8c. The terminal particle Reynolds number Re_t is 17.4, in good agreement with the values of 17.27 and 17.31 reported for two meshes of increasing resolution in [41] and the particle reaching the bottom of the channel around $t = 0.75t_0$



(a) Iso-contours of the dimensionless vorticity field $\frac{|\omega|l_0}{u_0}$. The values of the contours are 0, 2, 4,...,100.



(b) Temporal evolution of the cylinder vertical position.

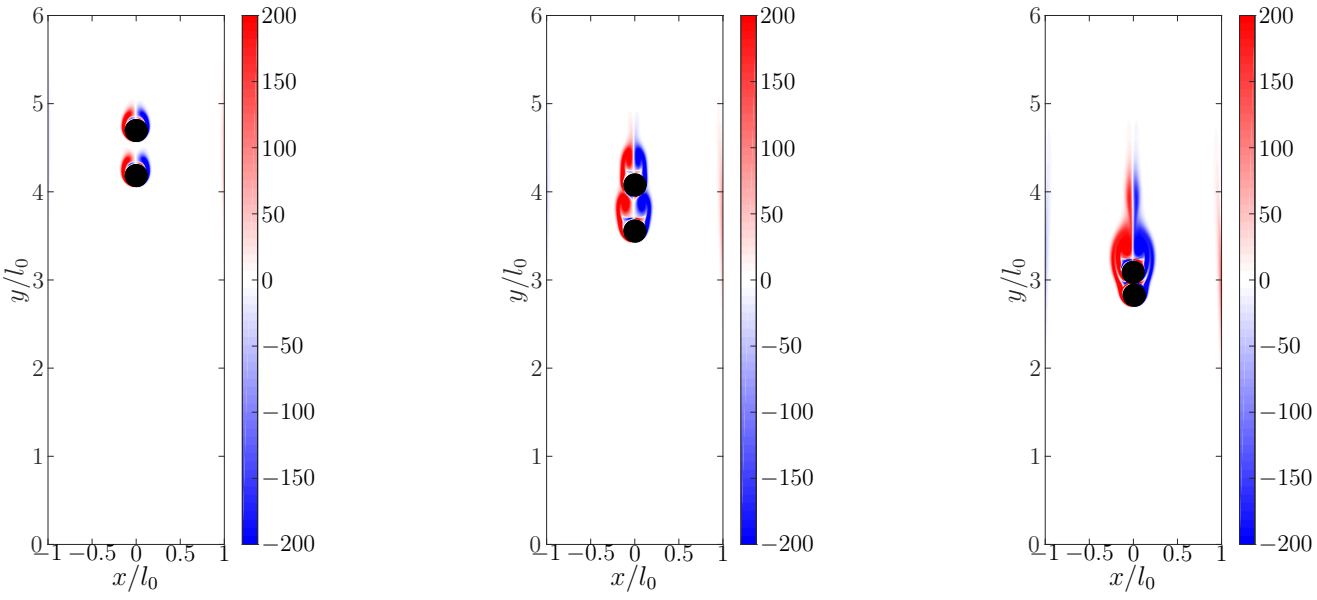


(c) Temporal evolution of the cylinder vertical velocity.

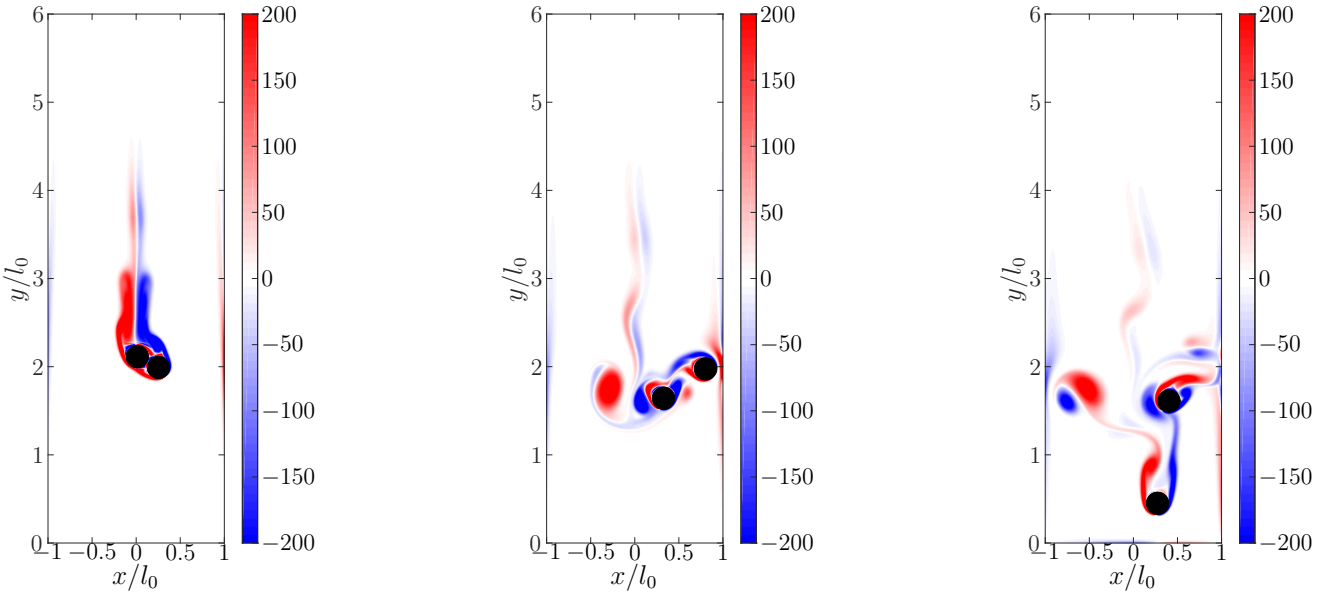
Figure 8: Sedimentation of a cylinder in a channel.

4.3. Drifting-Kissing-Tumbeling

The particle-particle interaction part of our method is validated by simulating the sedimentation of two circular particles sedimenting in a channel is simulated, using the results obtained by Glowinski et al. [41] as a reference. The geometrical parameters and reference quantities are identical to those described in the previous section. The solid density is here taken as $\rho_s = 1.5\rho$ and the kinematic viscosity is $\nu = 0.01(u_0 l_0)$. The two particles are initially positioned at $(0, 4.5)l_0$ and $(0, 5)l_0$. The flow field obtained at different dimensionless times is shown in Figure 9. The results obtained match well those obtained from Glowinski et al., with the kissing occuring around $t = 0.15t_0$, the tumbling between 0.15 and 0.2 t_0 and the final separation of the two particles.



(a) $t = 0.05\,t_0$ (b) $t = 0.10\,t_0$ (c) $t = 0.15\,t_0$



(d) $t = 0.20\,t_0$ (e) $t = 0.30\,t_0$ (f) $t = 0.40\,t_0$

Figure 9: Dimensionless vorticity field $\frac{\omega l_0}{u_0}$ around two circular particles sedimenting in a vertical channel highlighting the drifting-kissing-tumbeling phenomenon.

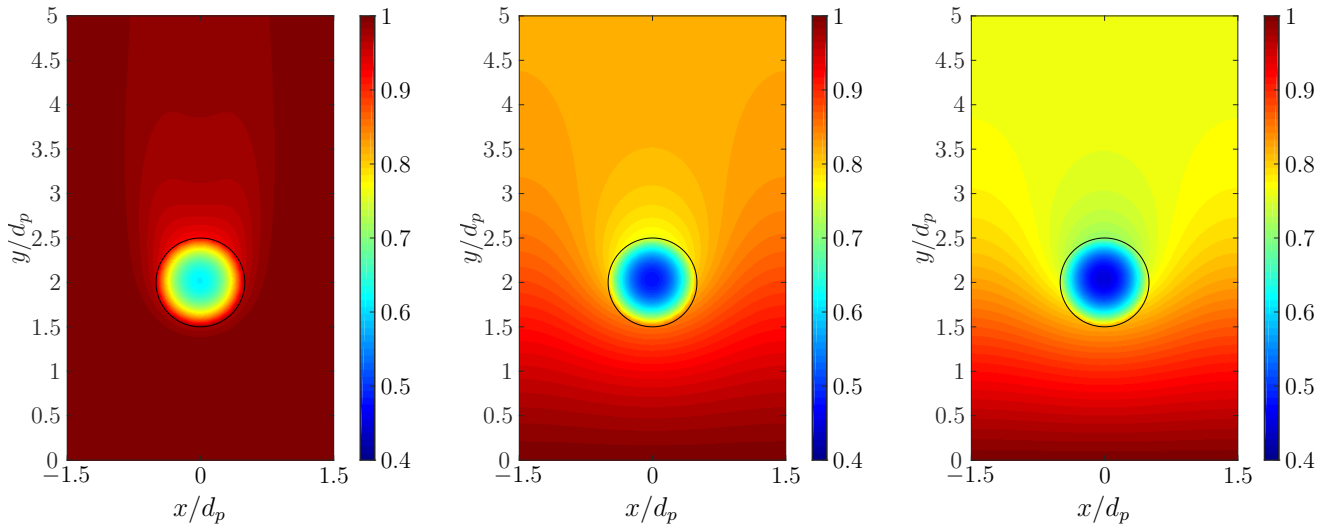
5. Reactive case studies

Depending on the level of approximation and on the comparison of the reaction and mass transfer time scales, different modeling approaches can be considered for the reaction part. In what follows, situations with solid-phase finite-rate volume reactions and infinite- or finite-rate surface

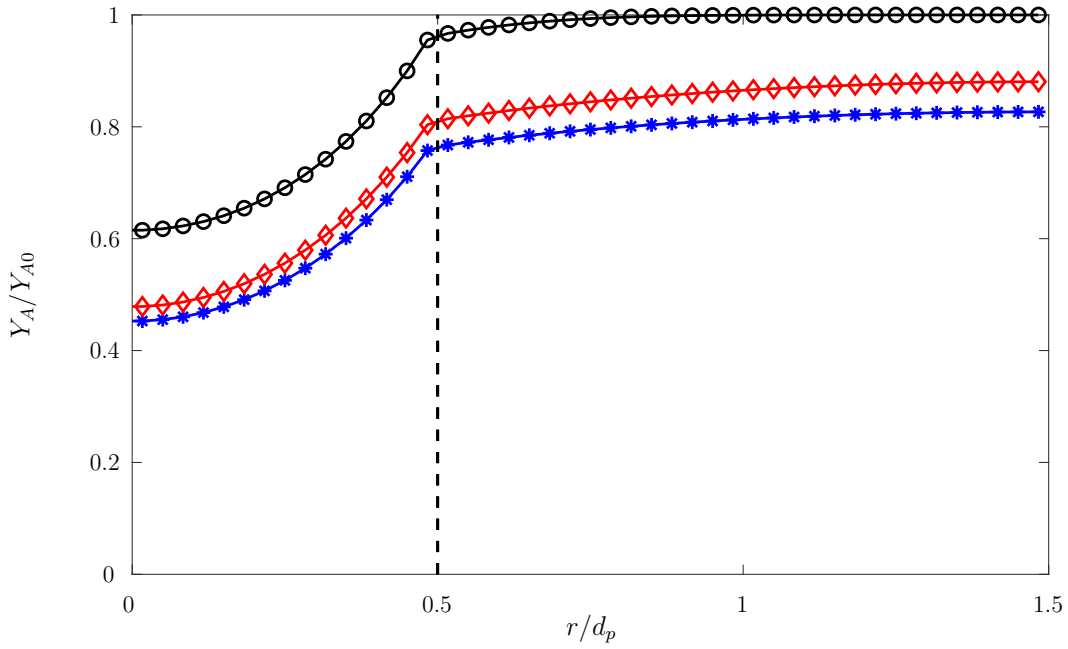
reactions are addressed. The impact of compressibility on mass and heat transfer is evaluated in the different cases. For all the subsequent simulations, the Schmidt number is fixed as $Sc = \frac{\mu_0}{\rho_0 \mathcal{D}} = Pr = 0.7$.

5.1. Intra-particle diffusion-reaction process

The first case considered is that of a finite rate catalytic reaction, with coupled heat and mass transfer between the solid and the fluid phase. The conservation of heat and mass fluxes at the surface of a particle is first verified. Considering a first-order catalytic reaction A $\longrightarrow$ B, the species transport Eq. (23) is integrated for A with the source terms $w_A = k\rho Y_A$, with k the rate constant with units [1/s]. The effective diffusivity of species in the solid phase is set to one tenth of the fluid-phase diffusivity ($\mathcal{D}_s = 0.1\mathcal{D}$) and the case of a volume Damköhler number $Da_V = \frac{kd_p^2}{\mathcal{D}_s} = 10$ is considered. The mass fraction fields obtained for $Re_p = 40$, $Re_p = 1$ and $Re_p = 0.5$ are shown in Fig. 10a, 10b and 10c respectively. These Reynolds numbers correspond to relevant conditions in fluidized beds, where the slip velocity between the gas and the particle may be very low for small particles at some locations in the bed. The mass fraction profile of species A along a radial cut is extracted in all cases (Fig. 10d) and the slope $\frac{\partial Y_A}{\partial n}$ is evaluated on the particle surface from the fluid and from the solid side. The ratio between these slopes must be the inverse of the diffusivity ratio to satisfy mass flux continuity at the particle surface: $-D\frac{\partial Y_A}{\partial n} = -D_s\frac{\partial Y_{A,s}}{\partial n}$, with $Y_{A,s}$ the mass fraction of A in the solid phase. For a resolution $d_p = 30h$, we obtain a slope ratio of 9.73 (2.7% error), 9.93 (0.7% error) and 9.94 (0.6% error) at $Re_p = 40$, $Re_p = 1$ and $Re_p = 0.5$, respectively. At lower Reynolds number, the conversion across one particle is increased, as a result of the longer effective contact time between the flow carrying the reacting species and the particle. It can also be observed that the intra-particle mass fraction field is nearly perfectly symmetric with respect to the particle center, justifying the classical 1-D radial description used in 1-D or CFD-DEM models. Yet, some symmetry breaking is observed with decreasing Re_p, suggesting a limited validity of this approximation for very low Re_p regimes.



(a) $Re_p = 40$ (b) $Re_p = 1$ (c) $Re_p = 0.5$



(d)

Figure 10: Forced convection coupled to intra-particle diffusion-reaction process; $\mathcal{D}_s = 0.1\mathcal{D}$, $Da_V = 10$, $Sc = 0.7$. (a, b, c) Mass fraction field Y_A/Y_{A0} (d) Mass fraction profile of species A along a horizontal cut through the particle center: $Re_p = 40$ ($-\circ$), $Re_p = 1$ ($-\diamond$) and $Re_p = 0.5$ ($-*$) .

5.2. Interfacial mass and heat transfer with infinitely fast reaction

In the case of a very fast irreversible reaction occurring in the solid phase, it can be assumed that the composition of the surface is virtually free of any reactant species. For the model reaction A $\longrightarrow$ B, this amounts to impose $Y_A = 0$ and $Y_B = 1$ on the particle surface. It follows that

the observed consumption rate of A over a particle, R_A in [kg/s], is determined by the interfacial transfer of A: $R_A = \dot{m}_{A,f\to s}$. The interfacial flux $\dot{m}_{A,f\to s}$ is obtained by integrating the penalization term over the volume of the particle:

$$\begin{aligned}\dot{m}_{A,f\to s} = \oint_{\partial\Omega_s} \mathbf{j}_A \cdot \hat{\mathbf{n}}\, dS &= \oint_{\partial\Omega_s} (\rho Y_k \mathbf{v}_k) \cdot \hat{\mathbf{n}} dS \\ &= -\int_{\Omega_s} \nabla \cdot (\rho Y_k \mathbf{v}_k)\, dV \\ &= \int_{\Omega_s} \rho \underbrace{\frac{DY_A}{Dt}}_{=0} dV + \int_{\Omega_s} \chi \left(\rho \frac{(Y_k - Y_{k,s})}{\Delta\tau}\right) dV \\ &= \int_{\Omega_s} \chi \left(\rho \frac{(Y_k - Y_{k,s})}{\Delta\tau}\right) dV. \end{aligned} \tag{44}$$

where the first term on the right-hand side vanishes because of the fixed surface composition.

If it is further assumed that the solid phase thermal conductivity is sufficiently large that it uniformizes its temperature in a time much smaller than the characteristic time of the fluid-solid heat transfer. The temperature of the solid phase is therefore considered as uniform and a global heat balance can be solved:

$$m_s c_{p,s} \dot{T}_s = Q_r + Q_{f\to s}, \tag{45}$$

with Q_r, the total heating rate (in [W]) induced by the reaction and computed as

$$Q_r = \sum_{k=1}^{N_s} R_k h_k, \tag{46}$$

and $Q_{f\to s}$, the interfacial heat flux. The latter is obtained after integration of the penalization term on the energy equation:

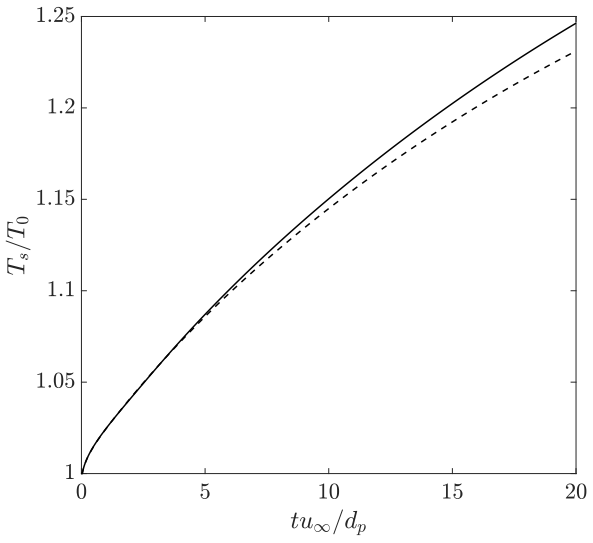
$$\begin{aligned} Q_{f\to s} = \oint_{\partial\Omega_s} \mathbf{q} \cdot \hat{\mathbf{n}}\, dS &= \oint_{\partial\Omega_s} \kappa \nabla T \cdot (-\hat{\mathbf{n}}) dS \\ &= \int_{\Omega_s} \nabla \cdot (\kappa \nabla T) dV \\ &= \int_{\Omega_s} \rho c_p \frac{DT}{Dt} dV + \int_{\Omega_s} \chi \left(\rho c_p \frac{(T - T_s)}{\Delta\tau}\right) dV \\ &= \dot{T}_s \int_{\Omega_s} \rho c_p dV + \int_{\Omega_s} \chi \left(\rho c_p \frac{(T - T_s)}{\Delta\tau}\right) dV. \end{aligned} \tag{47}$$

The combination of Eqs. (45) and (47) gives

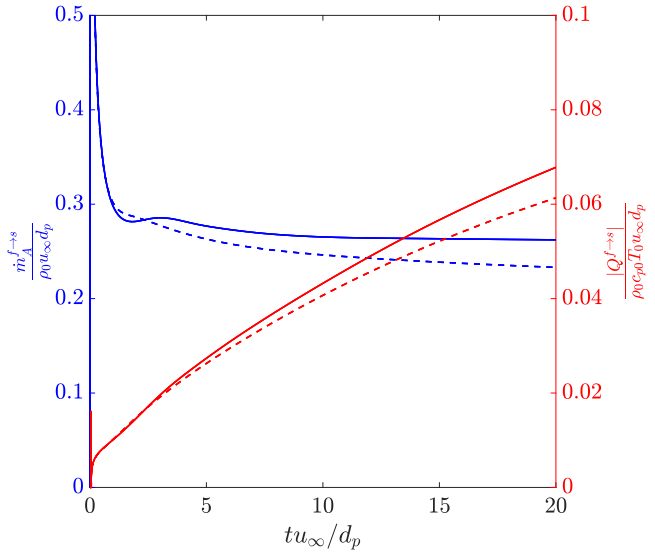
$$\dot{T}_s = \frac{\left(Q_r + \int_{\Omega_s} \chi \rho c_p \frac{(T - T_s)}{\Delta\tau} dV\right)}{\left(m_s c_{p,s} - \int_{\Omega_s} \rho c_p dV\right)}. \tag{48}$$

The value of T_s at the next time step is then used as the new Dirichlet condition in the penalization term of Eq. (15).

Considering an exothermic reaction, the increase of the particle temperature, T_s, with time is plotted in Fig. 11a for the enthalpies of formation $h_A = 0.5\,(c_{p,0}T_0)$, $h_B = 0$. The solid density ρ_s and specific heat $c_{p,s}$ are set equal to $10\rho_0$ and c_{p0}, respectively. It can be observed that T_s increases slower in the weakly compressible case. Because the intrinsic reaction rate is considered infinite, this can be attributed to the reduced mass transfer rate of reactant A from the fluid phase, as evidenced in Fig. 11b, hence reducing the consumption rate of A and the heat generation in the body of the particle. The heat transfer from the fluid phase is subsequently lowered, as a result of the decreased driving force $(T_s - T_0)$.



(a) Temporal evolution of the solid phase temperature.



(b) Temporal evolution of the heat and mass fluxes transferred from the fluid to the solid phase.

Figure 11: Infinitely fast and irreversible reaction A $\longrightarrow$ B with uniform solid phase temperature: incompressible (solid line) and weakly compressible (dashed line) cases. $Re_p = 40$, $Sc = Pr = 0.7$; $h_A = 0.5(c_{p0}T_0)$, $h_B = 0$; $\rho_s = 10\rho_0$, $c_{p,s} = c_{p0}$.

5.3. Interfacial mass transfer with finite rate surface reaction

An interesting application of the extension of the penalization method to Neumann- and Robin-type boundary conditions is the case of a surface reaction with finite rate chemistry. Considering, as in [42], an irreversible first order reaction in the absence of accumulation on the surface, the diffusion flux of the reacting species A at the solid surface balances exactly its rate of consumption:

$$\mathbf{j_A} \cdot \hat{\mathbf{n}} = -\rho \mathcal{D} \frac{\partial Y_A}{\partial n} = k_s \rho Y_A, \tag{49}$$

where k_s is the surface rate constant, with units [m/s] and the unit normal vector $\hat{\mathbf{n}}$ is pointing towards the interior of the solid phase.

Eq. (49) constitutes a Robin-type boundary condition on the particle surface for the species transport equation in the fluid. Indeed, it can be recast as

$$Da_S Y_A + d_p \frac{\partial Y_A}{\partial n} = 0, \tag{50}$$

with $Da_S = \frac{k_s d_p}{\mathcal{D}}$, the Damköhler number based on the surface reaction rate and the fluid diffusivity. Following the CBVP approach detailed in Section 2.2.2, the species transport Eq. (21) for a surface reaction is modified as

$$\frac{\partial Y_k}{\partial t} = (1-\chi)\left(-\mathbf{u}\cdot\nabla Y_k \; + \frac{1}{\rho}\nabla\cdot\left(\frac{\rho\mathcal{D}}{\overline{W}}\nabla\left(Y_k\overline{W}\right)\right)\right) - \frac{\chi}{\eta_c}\left(\left(\frac{Da_s}{d_p}\right)Y_A + \hat{\mathbf{n}}\cdot\nabla Y_k\right). \tag{51}$$

A drawback of the CBVP method for the implementation of Neumann- and Robin-type boundary conditions is the non-straightforward implicit integration of the penalization term. In contrast to the case where a Dirichlet boundary condition is prescribed, the penalization term is no longer local as it involves spatial derivatives of the solution. Hence, an explicit formulation of the penalization term must be used, making the constraint on the time step much stronger to guarantee an acceptable accuracy of the solution in the vicinity of the solid boundary. Typically, we found that the condition $\eta_c u_\infty \gtrsim \frac{u_\infty \Delta t}{h}$ had to be satisfied to ensure stability.

The generic surface reactions A $\longrightarrow$ B and A $\longrightarrow$ 2 B are investigated in a systematic manner. The penalization parameter η_c in Eq. (51) is fixed to $\eta_c = 0.1/u_\infty$. Fig. 12 shows the resulting mass fraction field of species A in the case of the equimolar surface reaction A $\longrightarrow$ B and for $Da_S = 1$.

The flow is simulated for different values of Da_S and the mass fraction profiles of A in the wake of the cylinder (through the particle center), are reported in Fig. 13a. As expected, with increasing Damköhler number, the effect of the surface reaction is more pronounced and the depletion of species A in the wake is more important. The case $Da_S = \infty$ corresponds to the situation of an infinitely fast reaction with zero mass fraction on the particle surface, leading to the Dirichlet boundary condition $Y_A = 0$. On the other hand, when $Da_S = 0$, the situation corresponds to an extremely fast diffusion process (or slow reaction) such that the species concentration gradients induced by the reaction are instantaneously smeared out, leading to a no-flux Neumann boundary condition: $\frac{\partial Y_A}{\partial n} = 0$.

For the reaction A $\longrightarrow$ 2 B, Fig. 13a also shows the effect of the molecular weight decrease on the consumption rate of reactant A. At low Da_S, the depletion of the reactant A is slightly more pronounced when the reaction is accompanied with volume expansion (A $\longrightarrow$ 2 B) while at higher Da_S, when diffusion becomes the rate-limiting process, the trend reverses and the volume expansion results in a lower conversion of A than the equimolar case A $\longrightarrow$ B.

Fig. 13b shows the mass fraction profile perpendicular to the flow (vertical cut through the particle center in Fig. 12) obtained inside and outside the particle. The hyperbolic region where the characteristics are propagated and the diffusive region which acts as a support to the solution are clearly evidenced.

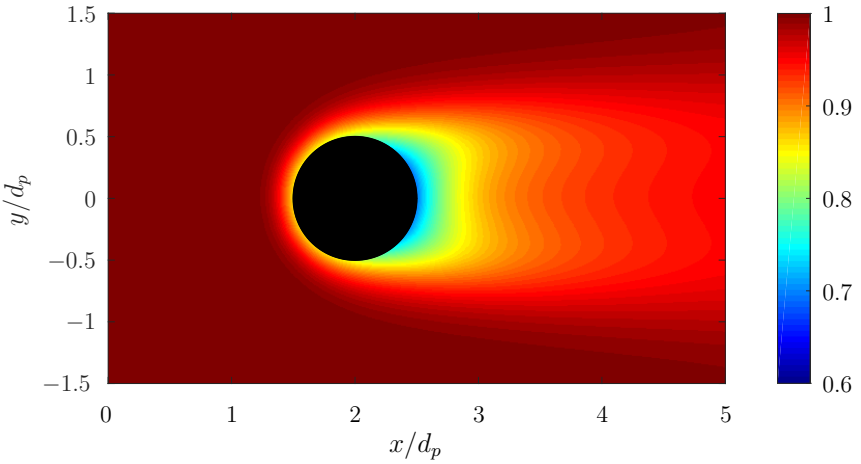
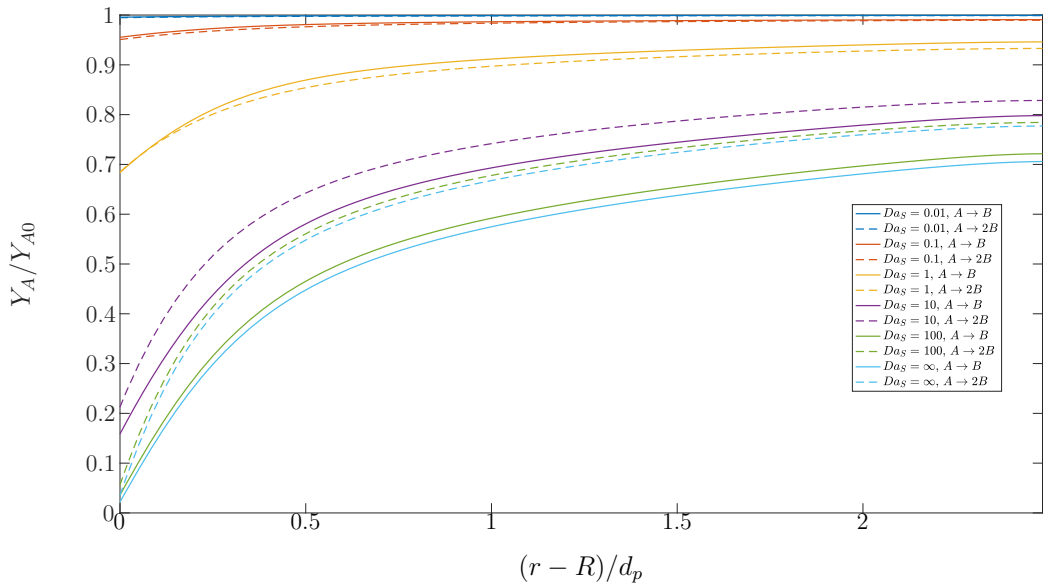
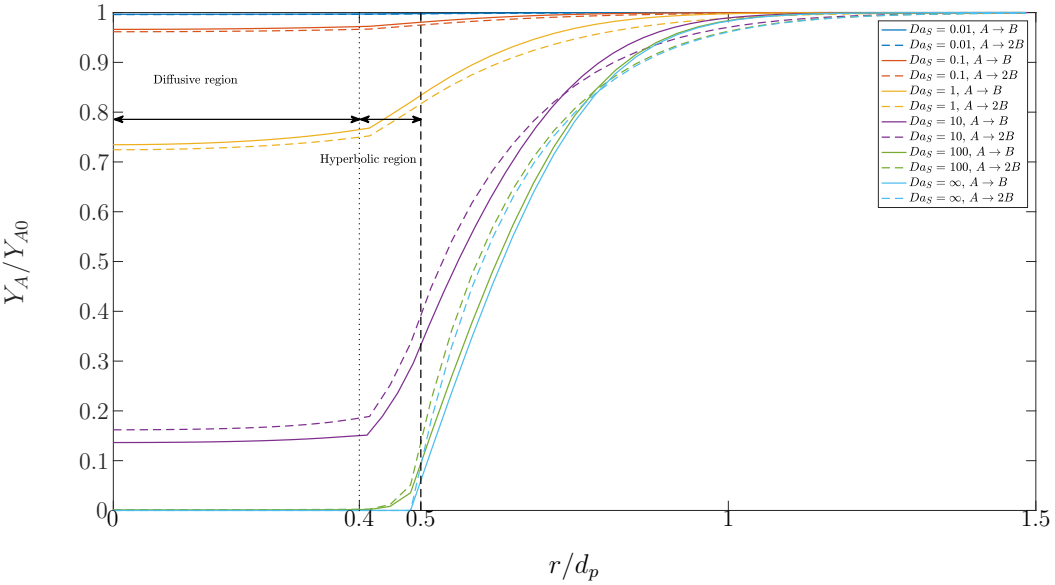


Figure 12: Iso-contours of Y_A/Y_{A0} for a surface reaction A $\longrightarrow$ B and with $Da_S = 1$. $Re_p = 40$, $Sc = 0.7$.



(a) Mass fraction profile of species A in the wake of the particle (horizontal cut through the particle center).



(b) Mass fraction profile of species A along a vertical cut through the particle center with finite-rate surface reaction.

Figure 13: Surface reactions A $\longrightarrow$ B and A $\longrightarrow$ 2 B at different Da_S; $Re_p = 40$, $Sc = 0.7$.

6. Conclusion

In this work, a new combination of the weakly compressible approximation and the Brinkman penalization method was developed. The method was validated against literature benchmarks at different particle Reynolds numbers, in static and moving configurations. Different situations encountered in reacting gas-solid flows were subsequently addressed. Using the classical formulation of the penalization method for Dirichlet-type boundary conditions, we performed a set of numeri-

cal experiments with increasing values for the solid phase temperature, highlighting the decrease of the heat transfer rate and the increase of the drag coefficient relatively to the incompressible case. The situation where the external flow is coupled to an intra-particle diffusion-reaction process was simulated for different particle Reynolds numbers corresponding to relevant conditions in industrial fluidized beds. The reduction of the slip velocity based Reynolds number induced by the fluidization regime was shown to improve the usage of the catalytic phase, and hence the conversion. It appeared that the classically used 1-D radial approximation for the intra-particle species profiles was fairly well verified down to $Re_p = 0.5$. Yet, the asymmetry inside the particle increases with decreasing Re_p and it can be expected that at locations in the bed where the slip velocity is very low, this approximation will be less valid. The case of an infinitely fast catalytic reaction with subsequent heat release in the solid phase and considering a high solid thermal conductivity was then studied. It showed a reduced mass transfer rate from the fluid to the solid phase because of the reduced density of the fluid surrounding the particle, resulting in a slower increase of the solid phase temperature. The imposition of Neumann- and Robin-type boundary conditions was performed using the characteristic based volume penalization (CBVP) method developed by Brown-Dymkoski et al. [22]. It allowed to treat the interesting case of finite-rate surface reactions. It was shown that the decrease of the fluid density induced by composition modifications tends to reduce the conversion of the reactant in the wake of the particle when diffusion becomes the rate-limiting phenomenon. This effect would also appear in cases where the fluid goes through an array of particles, like in fixed bed reactors. Future work will be dedicated to the efficient three-dimensional implementation of the method so as to build new meso-scale models for static (fixed bed) and moving (fluidized bed) configurations.

Acknowledgments

Baptiste Hardy is a Research Fellow of the Fonds de la Recherche Scientifique - FNRS, under grant n°1.A.700.18F. This work was completed thanks to the computational resources provided by the Consortium des Equipements de Calcul Intensif (CÉCI).

References

[1] N. G. Deen, J. Kuipers, Direct numerical simulation of fluid flow accompanied by coupled mass and heat transfer in dense fluid-particle systems, Chemical Engineering Science 116 (2014) 645–656.

[2] H. H. Hu, N. A. Patankar, M. Y. Zhu, Direct numerical simulations of fluid-solid systems using the Arbitrary Lagrangian-Eulerian technique, Journal of Computational Physics 169 (2) (2001) 427–462.

[3] R. Mittal, G. Iaccarino, Immersed Boundary Methods, Annual Review of Fluid Mechanics 37 (2005) 239–261.

[4] C. S. Peskin, Flow patterns around heart valves: A numerical method, Journal of Computational Physics 10 (2) (1972) 252–271.

[5] M. Uhlmann, An immersed boundary method with direct forcing for the simulation of particulate flows, Journal of Computational Physics 209 (2) (2005) 448–476.

[6] S. Majumdar, G. Iaccarino, P. Durbin, RANS solvers with adaptive structured boundary non-conforming grids, Annual Research Briefs, Center for Turbulence Research, Stanford University (2001) 353–466.

[7] D. K. Clarke, H. A. Hassan, M. D. Salas, Euler calculations for multielement airfoils using Cartesian grids, AIAA Journal 24 (3) (1986) 353–358.

[8] R. Mittal, C. Bonilla, H. S. Udaykumar, Cartesian grid methods for simulating flows with moving boundaries, Transactions on Modelling and Simulation 33 (2003) 557–566.

[9] X. Shao, Y. Shi, Z. Yu, Combination of the fictitious domain method and the sharp interface method for direct numerical simulation of particulate flows with heat transfer, International Journal of Heat and Mass Transfer 55 (23-24) (2012) 6775–6785.

[10] M. Sulaiman, A. Hammouti, E. Climent, A. Wachs, Coupling the fictitious domain and sharp interface methods for the simulation of convective mass transfer around reactive particles: Towards a reactive Sherwood number correlation for dilute systems, Chemical Engineering Science 198 (2019) 334–351.

[11] E. Arquis, J. P. Caltagirone, Sur les conditions hydrodynamiques au voisinage d'une interface milieu fluide-milieu poreux: application à la convection naturelle, CR Acad. Sci. Paris II 299 (1984) 1–4.

[12] P. Angot, C. H. Bruneau, P. Fabrie, A penalization method to take into account obstacles in incompressible viscous flows, Numerische Mathematik 81 (1999) 497–520.

[13] D. Kolomenskiy, K. Schneider, A Fourier spectral method for the Navier-Stokes equations with volume penalization for moving solid obstacles, Journal of Computational Physics 228 (16) (2009) 5687–5709.

[14] B. Kadoch, D. Kolomenskiy, P. Angot, K. Schneider, A volume penalization method for incompressible flows and scalar advection-diffusion with moving obstacles, Journal of Computational Physics 231 (12) (2012) 4365–4383.

[15] M. Gazzola, P. Chatelain, W. M. van Rees, P. Koumoutsakos, Simulations of single and multiple swimmers with non-divergence free deforming geometries, Journal of Computational Physics 230 (19) (2011) 7093–7114.

[16] Q. Liu, O. Vasilyev, A Brinkman penalization method for compressible flows in complex geometries, Journal of Computational Physics 227 (2007) 946–966.

[17] O. Boiron, G. Chiavassa, R. Donat, A high-resolution penalization method for large Mach number flows in the presence of obstacles, Computers and Fluids 38 (3) (2009) 703–714.

[18] A. Majda, J. Sethian, The derivation and numerical solution of the equations for zero Mach number combustion, Combustion Science and Technology 42 (3-4) (1985) 185–205.

[19] A. Abdelsamie, G. Fru, T. Oster, F. Dietzsch, G. Janiga, D. Thévenin, Towards direct numerical simulations of low-Mach number turbulent reacting and two-phase flows using immersed boundaries, Computers and Fluids 131 (2016) 123–141.

[20] A. W. Cook, J. J. Riley, Direct numerical simulation of a turbulent reactive plume on a parallel computer, Journal of Computational Physics 129 (2) (1996) 263–283.

[21] T. Poinsot, D. Veynante, Theoretical and Numerical Combustion, R.T. Edwards, 2005.

[22] E. Brown-Dymkoski, N. Kasimov, O. V. Vasilyev, A characteristic based volume penalization method for general evolution problems applied to compressible viscous flows, Journal of Computational Physics 262 (2014) 344–357.

[23] H. N. Najm, P. S. Wyckoff, O. M. Knio, A semi-implicit numerical scheme for reacting flow I, Journal of Computational Physics 402 (1998) 381–402.

[24] B. Lessani, M. V. Papalexandris, Time-accurate calculation of variable density flows with strong temperature gradients and combustion, Journal of Computational Physics 212 (1) (2006) 218–246.

[25] A. Tyliszczak, High-order compact difference algorithm on half-staggered meshes for low Mach number flows, Computers and Fluids 127 (2016) 131–145.

[26] R. Knikker, A comparative study of high-order variable property segregated algorithms for unsteady low Mach number flow, International Journal for Numerical Methods in Fluids 66 (2011) 403–427.

[27] A. J. Chorin, A numerical method for solving incompressible viscous flow problems, Journal of Computational Physics 2 (1) (1967) 12 – 26.

[28] E. Motheau, J. Abraham, A high-order numerical algorithm for DNS of low-Mach-number reactive flows with detailed chemistry and quasi-spectral accuracy, Journal of Computational Physics 313 (2016) 430–454.

[29] F. Nicoud, Conservative high-order finite-difference schemes for low-Mach number flows, Journal of Computational Physics 158 (2000) 71–97.

[30] D. J. Tritton, Experiments on the flow past a circular cylinder at low Reynolds numbers, Journal of Fluid Mechanics 6, (1959) 547–567.

[31] M. Coutanceu, R. Bouard, Experimental determination of the main features of the viscous flow in the wake of a circular cylinder in uniform translation, Journal of Fluid Mechanics 79 (1977) 231–256.

[32] P. Bigay, G. Oger, P.-M. Guilcher, D. Le Touzé, A weakly-compressible Cartesian grid approach for hydrodynamic flows, Computer Physics Communications 220 (2017) 31–43.

[33] D. Canuto, K. Taira, Two-dimensional compressible viscous flow around a circular cylinder, Journal of Fluid Mechanics 785 (2015) 349–371.

[34] M. N. Linnick, H. F. Fasel, A high-order immersed interface method for simulating unsteady incompressible flows on irregular domains, Journal of Computational Physics 204 (1) (2005) 157–192.

[35] S. C. R. Dennis, G.-Z. Chang, Numerical solutions for steady flow past a circular cylinder at Reynolds numbers up to 100, Journal of Fluid Mechanics 42 (03) (1970) 471.

[36] J. M. Macha, Drag of circular cylinders at transonic Mach numbers, Journal of Aircraft 14 (6) (1977) 605–607.

[37] S. W. Churchill, M. Bernstein, A correlating equation for forced convection from gases and liquids to a circular cylinder in crossflow, Journal of Heat Transfer 99 (2) (1977) 300.

[38] R. Mittal, H. Dong, M. Bozkurttas, F. M. Najjar, A. Vargas, A. von Loebbecke, A versatile sharp interface immersed boundary method for incompressible flows with complex boundaries, Journal of Computational Physics 227 (10) (2008) 4825–4852.

[39] S. V. Apte, M. Martin, N. A. Patankar, A numerical method for fully resolved simulation (FRS) of rigid particle flow interactions in complex flows, Journal of Computational Physics 228 (8) (2009) 2712–2738.

[40] Z. G. Feng, E. E. Michaelides, Proteus: A direct forcing method in the simulations of particulate flows, Journal of Computational Physics 202 (1) (2005) 20–51.

[41] R. Glowinski, T. W. Pan, T. I. Hesla, D. D. Joseph, J. Périaux, A fictitious domain approach to the direct numerical simulation of incompressible viscous flow past moving rigid bodies: Application to particulate flow, Journal of Computational Physics 169 (2) (2001) 363–426.

[42] J. Lu, S. Das, E. A. Peters, J. Kuipers, Direct numerical simulation of fluid flow and mass transfer in dense fluid-particle systems with surface reactions, Chemical Engineering Science 176 (2018) 1–18.